Optical Dimer Excitations and Exchange Parameters in $(Et_4N)_3Cr_2F_9$: First Observation of the $^4A_2 \rightarrow {}^2A_1$ Transition

Ralph Schenker,[†] Stephan Heer,[†] Hans U. Güdel,*[,†] and Høgni Weihe[‡]

Departement für Chemie und Biochemie, Universität Bern, Freiestrasse 3, CH-3000 Bern 9, Switzerland, and H. C. Ørsted Institutet, Københavns Universitet, Universitetsparken 5, DK-2100 København Ø, Denmark

Received July 11, 2000

The synthesis, crystal growth, and polarized optical absorption spectra in the visible and near-UV of $(Et_4N)_3Cr_2F_9$ are reported. In the energy range 25800−27700 cm^{-1} the $^4A_2 \rightarrow {}^2A_1$ (*O* notation) ligand field transition can be resolved in detail for the first time in any Cr^{3+} compound. This allows the determination of the antiferromagnetic ground-state exchange splitting with great accuracy: $J = 25.9$ cm^{-1} and $j = 0.27$ cm^{-1} using the Hamiltonian $H = J(\mathbf{S_A}\cdot\mathbf{S_B}) - j(\mathbf{S_A}\cdot\mathbf{S_B})^2$, where j leads to deviations from the regular Landé pattern. The temperature dependence of the magnetic susceptibility is nicely reproduced by these parameters. A comparison with $Cs_3Cr_2Cl_9$ and $Cs_3Cr_2Br_9$ reveals an exponential dependence of the ground-state splitting upon the Cr−Cr distance in the $[Cr_2X_9]^{3-}$ dimers. This is the result of a dominant σ-type orbital exchange pathway along the Cr−Cr axis.

1. Introduction

A very wide range of Cr^{3+} compounds containing exchange-coupled Cr^{3+} pairs have been investigated by optical spectroscopy within the past decades. Exchange splittings in the ground and excited states are usually derived from analysis of the spin-forbidden transitions within the ground electron configuration, $^4A_2 \leftrightarrow {}^2E$, $^2T_1$, because they often consist of sharp lines and can be observed both in absorption and in emission. In a dimer these excited states are called singly excited states because formally only one of the two centers is excited. Several studies on Cr^{3+} pairs in doped oxide lattices such as ruby,[1,2] $LaAlO_3$,[3] $YAlO_3$,[4] and spinels[5−7] belong to the pioneering work. A great deal of work has been done on a number of molecular mono-,[8] di-,[9−12] and tri-μ-hydroxo[13,14] bridged Cr^{3+} dimers. The most accurate determination of exchange splittings using optical spectroscopy so far was possible in the triply bridged $[Cr_2(OH)_3(tmtacn)_2](ClO_4)_3$.[15] Also systems of the type $A_3Cr_2X_9$ (A = Cs, Rb; X = Cl, Br, I) have been investigated in detail.[16−21] However, the corresponding fluorides remained unexplored so far, maybe because of difficulties in their preparation. So far, exchange splittings have been derived from the analysis of $^4A_2 \rightarrow {}^2E$, $^2T_1$ transitions. The observation of the $^4A_2 \rightarrow {}^2A_1$ (*O* notation) excitation in any Cr^{3+} compound has not been reported so far.

In this study we present the syntheses and growth of single crystals of $(Et_4N)_3Cr_2F_9$, which allows us to extend the research on Cr^{3+} dimers to fluoride systems. The synthesis procedure differs substantially from the one for $(Me_4N)_3Cr_2F_9$ reported in ref 22. We report polarized optical absorption spectra of single crystals between 13 000 and 45 000 cm^{-1} at various temperatures. The $^4A_2 \rightarrow {}^2A_1$ ligand field transition is resolved and analyzed in detail, allowing an accurate determination of exchange splittings and the resulting exchange parameters. The temperature dependence of the magnetic susceptibility turns out to be nicely reproduced by these parameters. The results are compared with those of the corresponding chloride and bromide systems, allowing us to follow and rationalize the trend of magnetic properties along the series of face-sharing $[Cr_2F_9]^{3-}$, $[Cr_2Cl_9]^{3-}$, and $[Cr_2Br_9]^{3-}$ dimers.

2. Experimental Section

2.1. Synthesis and Crystal Structure. All the chemicals used for the present study were at least of reagent grade. The title complex was synthesized using Schlenk technique throughout. A dry solution of Et_4NF in ethanol was obtained by distilling half of the water/ethanol off from a solution of 55 g (0.3 mol) of $Et_4NF\cdot 2H_2O$ in 400 mL of dry ethanol. After this step was repeated three times, 100 mL of ethanol and 100 mL of benzene were added in the last run, and the solution

* To whom correspondence should be addressed. E-mail: hans-ulrich.guedel@iac.unibe.ch. Fax: +41 31 631 43 99.
† Universität Bern.
‡ Københavns Universitet.

(1) Naito, M. *J. Phys. Soc. Jpn* **1973**, *34*, 1491.
(2) van der Ziel, J. P. *Phys. Rev. B* **1974**, *9*, 2846.
(3) van der Ziel, J. P. *Phys. Rev. B* **1971**, *4*, 2888.
(4) van der Ziel, J. P. *J. Chem. Phys.* **1972**, *57*, 2442.
(5) van Gorkom, G. G. P.; Henning, J. C. M.; van Stapele, R. P. *Phys. Rev. B* **1973**, *8*, 955.
(6) van der Boom, H.; van Dijsseldonk, J. J.; Henning, J. C. M. *J. Chem. Phys.* **1977**, *66*, 2368.
(7) Henning, J. C. M. *Phys. Rev. B* **1980**, *21*, 4983.
(8) Riesen, H.; Güdel, H. U. *Inorg. Chem.* **1986**, *25*, 3566.
(9) Schönherr, T. *J. Mol. Struct.: THEOCHEM* **1992**, *261*, 203.
(10) Decurtins, S.; Güdel, H. U.; Pfeuti, A. *Inorg. Chem.* **1982**, *21*, 1101.
(11) Decurtins, S.; Güdel, H. U. *Inorg. Chem.* **1982**, *21*, 3598.
(12) Reber, C.; Güdel, H. U.; Spiccia, L.; Marty, W. *Inorg. Chem.* **1987**, *26*, 3186.
(13) Schenker, R.; Weihe, H.; Güdel, H. U. *Chem. Phys. Lett* **1999**, *303*, 229.
(14) Schenker, R.; Weihe, H.; Güdel, H. U. *Inorg. Chem.* **1999**, *38*, 5593.
(15) Riesen, H.; Güdel, H. U. *Mol. Phys.* **1987**, *60*, 1221.
(16) Briat, B.; Russel, M. F.; Rivoal, J. C.; Chapelle, J. P.; Kahn, O. *Mol Phys.* **1977**, *34*, 1357.
(17) Dubicki, L.; Ferguson, J.; Harrowfield, B. *Mol. Phys.* **1977**, *34*, 1545.
(18) Johnstone, I. W.; Maxwell, K. J.; Stevens, K. W. H. *J. Phys. C: Solid State Phys.* **1981**, *14*, 1297.
(19) Dean, N. J.; Maxwell, K. J.; Stevens, K. W. H.; Turner, R. J. *J. Phys. C: Solid State Phys.* **1985**, *18*, 4505.
(20) Dean, N. J.; Maxwell, K. J. *Mol. Phys.* **1982**, *47*, 551.
(21) Ferrigato, A.; Maxwell, K. J. *J. Phys. Chem. Solids* **1990**, *51*, 157.
(22) Kiriazis, L.; Mattes, R. *Z. Anorg. Allg. Chem.* **1991**, *593*, 90.

10.1021/ic000759b CCC: $20.00
Published on Web 02/27/2001

was concentrated to 240 mL (1.25 M). An amount of 1.50 g (4 mmol) of $Cr(thf)_3Cl_3$ (for preparation see ref 23) was dissolved in 50 mL of dry DMF. After the solution was heated to 70 °C, an amount of 22.5 mL (18 mmol) of Et_4NF ethanolic solution was added. The fast formation of the $[Cr_2F_9]^{3-}$ complex is indicated by a color change from green to brownish-yellow. After being concentrated to 24 mL, the solution was allowed to cool slowly from 130 °C to room temperature within 48 h. The resulting brown needles were filtered off and dried under vacuum. The product with formula $(Et_4N)_3Cr_2F_9$ is very hygroscopic; it decomposes completely within minutes when exposed to air. The crystals were thus stored and handled in a dry box under nitrogen atmosphere. The purity of the bulk material was checked by powder X- ray diffraction and comparison with the single-crystal structural data.

We solved the crystal structure of $(Et_4N)_3Cr_2F_9$ at room temperature.[24] The compound crystallizes in the hexagonal space group $P6_3/m$, with $a = 13.272$ Å and $c = 10.723$ Å. The Cr^{3+} single ion and dimer symmetries are exactly C_3 and C_{3h}, respectively, with the 3-fold axis lying parallel to the hexagonal crystal c axis. The Cr−Cr distance is 2.769 Å.

2.2. Optical Absorption Measurements. Polarized crystal absorption spectra were measured in the spectral range 770−220 nm in both σ and π polarization, i.e., with the electric vector of the light perpendicular and parallel to the c axis, respectively. The hexagonal prisms with typical dimensions of 0.25 mm in diameter and 0.5 mm in length were ideal for absorption measurements on the long wavelength side of 580 nm. For measurements at shorter wavelengths a single crystal was ground to a thin disk containing the c axis with the dimensions $370 \times 150 \times 105\ \mu m^3$. For the measurement of the intense π-polarized band between 555 and 400 nm a $(Et_4N)_3Fe_2F_9$ crystal doped with 6% Cr^{3+} was used. The measurements of the very weak bands between 390 and 360 nm were achieved using one of the largest crystals with a thickness of 950 μm. Absorption spectra in the visible and UV were recorded on a Cary 05e double-beam spectrometer. Variable sample temperatures between 10 and 300 K were achieved using a closed-cycle helium refrigerator (Air Products).

2.3. Magnetic Measurements. Variable-temperature dc magnetic susceptibility measurements on powdered samples were carried out in the temperature range 300−2 K at a magnetic field of 0.1 T using a magnetometer (Quantum Design MPMS-XL-5) equipped with a superconducting quantum interference device (SQUID) sensor.

3. Results

The σ- and π-polarized 10 K survey absorption spectra of $(Et_4N)_3Cr_2F_9$ in the visible and near-UV are shown in Figure 1. The bands are designated in *O* notation. Since the crystal was slightly too thick, the π-polarized bands above 30 000 cm^{-1} suffer from stray-light effects, generating the noise on the top of the $^4T_{1b}$ band and the onset to the charge transfer (CT) bands above 44 000 cm^{-1}. The intense $^4T_1$ band between 18 000 and 25 000 cm^{-1} was thus measured using a $(Et_4N)_3Fe_2F_9$ crystal doped with 6% Cr^{3+} because pure $(Et_4N)_3Fe_2F_9$ is transparent below 25 000 cm^{-1}. The Cr^{3+}:$(Et_4N)_3Fe_2F_9$ spectrum was scaled to the π spectrum of pure $(Et_4N)_3Cr_2F_9$ using the intensities of the $^4T_2$ band. Throughout the visible and near-UV the intensity is larger in π than in σ polarization. Transitions to the ^2E and $^2T_1$ states are observed as weak and sharp features superimposed on the high-energy side of the $^4T_2$ band. A special feature are the dips near the top of the $^4T_{1a}$ band. These characteristic antiresonance features are due to interference between the vibrational sideband of the $^4T_{1a}$ and several levels of the $^2T_2$ state. Four dips are seen in each polarization. There are some weak features built on the low-energy side of the $^4T_{1b}$ band in σ polarization, which we assign to double excitations to $^2E^2E$, $^2E^2T_1$, and $^2T_1{}^2T_1$ (see Figure 1).

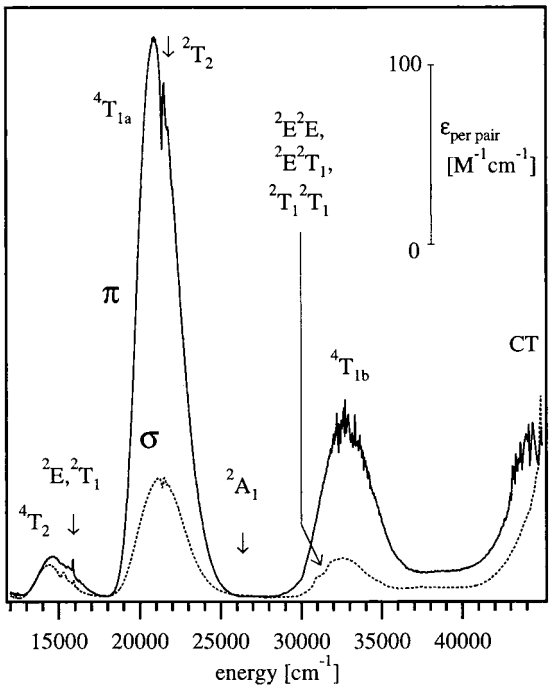

Figure 1. The σ- and π-polarized 10 K survey absorption spectra in the visible and near-UV of a single crystal of $(Et_4N)_3Cr_2F_9$. The bands are designated in *O* notation. The π spectrum from 18 000 to 25 000 cm^{-1} containing the intense $^4T_{1a}$ band was obtained from a $(Et_4N)_3Fe_2F_9$ crystal doped with 6% Cr^{3+} and scaled to the spectrum of the undiluted crystal by the $^4T_2$ absorption.

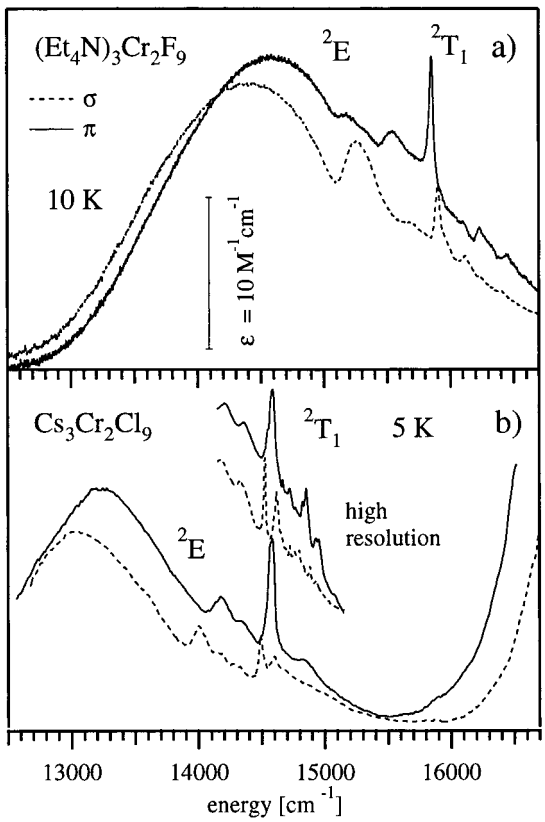

Figure 2. (a) The σ- and π-polarized 10 K absorption spectra of $(Et_4N)_3Cr_2F_9$ in the region of the $^4A_2 \rightarrow {}^4T_2$, ^2E, $^2T_1$ excitations. (b) Corresponding 5 K spectra of $Cs_3Cr_2Cl_9$ adapted from refs 16 and 17.

The σ- and π-polarized 10 K absorption spectra between 12 500 and 16 700 cm^{-1} are enlarged in Figure 2a. The maximum of the $^4T_2$ band is shifted by 230 cm^{-1} to lower

(23) Herwig, W.; Zeiss, H. H. *J. Org. Chem.* **1977**, *16*, 2534.
(24) Results will be published separately.

Table 1. Energies, Polarizations, Temperatures, Oscillator Strengths, and Assignments of the Observed Electronic Pair Transitions to the $^2T_1$ State[a]

energy, cm^{-1}	polarization	temp, K	f	assignment
15 795	π	60	4.0×10^{-6}	$^4A_2$ ($S = 2$) → 15 876 ($^2T_1$)
15 837	π	20	1.2×10^{-6}	$^4A_2$ ($S = 1$) → 15 865 ($^2T_1$)
15 851	π	10	1.6×10^{-6}	$^4A_2$ ($S = 0$) → 15 851 ($^2T_1$)
15 860	σ	40	4.3×10^{-7}	$^4A_2$ ($S = 1$) → 15 888 ($^2T_1$)
15 900	σ	10	7.9×10^{-7}	$^4A_2$ ($S = 0$) → 15 900 ($^2T_1$)
15 900	σ	40	3.5×10^{-7}	$^4A_2$ ($S = 1$) → 15 928 ($^2T_1$)

[a] Oscillator strengths are corrected for the appropriate Boltzmann population. The S values refer to the dimer ground-state levels.

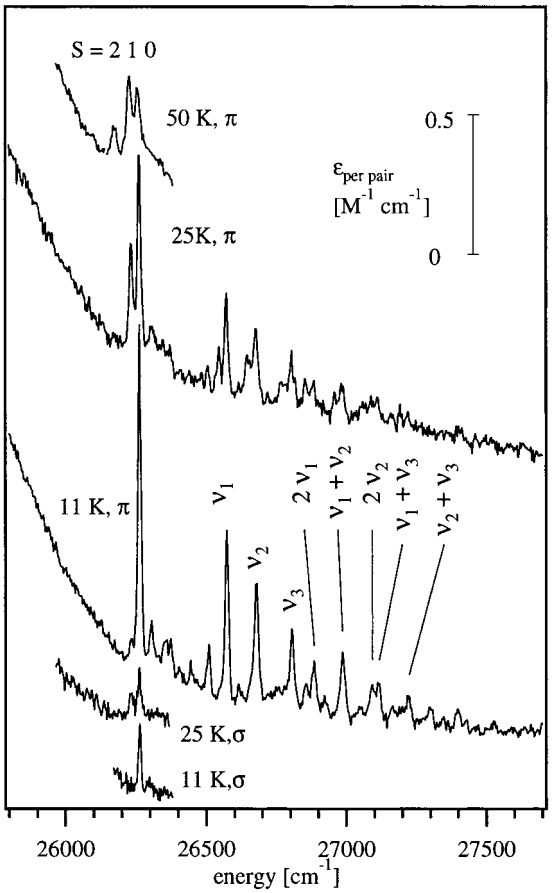

Figure 3. The π (top three traces) and σ (bottom two traces) polarized absorption spectra in the $^4A_2 \rightarrow {}^2A_1$ region at three different temperatures as indicated. The S values of the three origin lines at the top indicate the spin of the initial ground-state level. ν_1, ν_2, and ν_3 denote the three major vibrational modes involved in the sideband structure.

energy in σ compared to π polarization. The features built on the $^4T_2$ band above 14 500 cm^{-1} are due to $^4A_2 \rightarrow {}^2E$, $^2T_1$ transitions. Between 14 800 and 15 700 cm^{-1} there are broad and temperature-independent antiresonances that are more pronounced in σ polarization. Around 15 900 cm^{-1} some prominent, overlapping cold and hot (not shown) absorption bands occur that are completely polarized. Three different temperature dependences are recognized upon heating (not shown). Above 16 000 cm^{-1} there are several weak and mostly π-polarized bands. Band energies, polarizations, and intensities of this spectral region are listed in Table 1.

Figure 3 shows the σ- and π-polarized absorption spectra from 25 800 to 27 700 cm^{-1} at different temperatures as indicated. The overall intensity of these bands is so weak that they are not seen in the survey spectra of Figure 1. It is an order of magnitude larger in π (upper three spectra) than in σ polarization

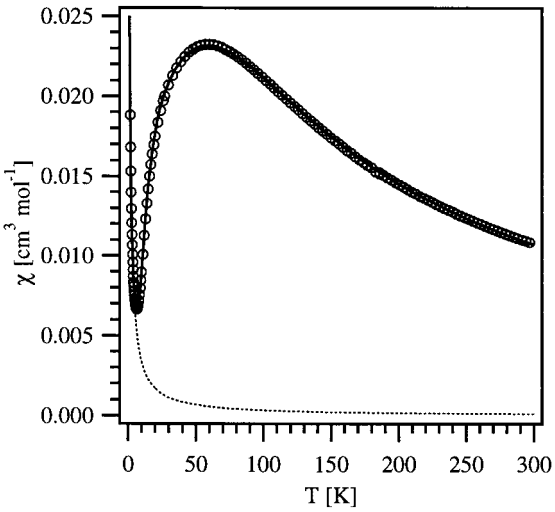

Figure 4. Magnetic susceptibility curve of a polycrystalline sample of $(Et_4N)_3Cr_2F_9$ in the range 2−300 K (circles). The solid line was obtained with eq 5, and the fixed parameter values $E_1 = 27.6$ cm^{-1}, $E_2 = 81.2$ cm^{-1}, and $E_3 = 157.8$ cm^{-1} were obtained from the analysis of the $^4A_2 \rightarrow {}^2A_1$ pair transitions. The parameter values $g = 2.00$ and $C = 0.0337$ cm^3 K mol^{-1} were adjusted to fit the experimental data. The dotted curve indicates the susceptibility induced by paramagnetic impurity.

(bottom two spectra). At 11 K there is a prominent sharp origin band designated $S = 0$ at 26 262.9 cm^{-1}, with a number of weaker sidebands at higher energy. At higher temperatures two hot origin bands designated $S = 1$ and 2 arise at 26 235.3 and 26 181.7 cm^{-1}, respectively.

The molar magnetic susceptibility curve of a polycrystalline sample in the range 300−2 K is shown in Figure 4. χ shows a continuous increase upon cooling, reaching a broad maximum around 60 K, indicating antiferromagnetic interaction. Below 6 K it rises sharply because of paramagnetic impurities in the sample.

4. Analysis and Discussion

4.1. Trigonal Ligand Field. In a trigonal ligand field the t_2 orbitals are split into two sets of orbitals t_0 and t_+, t_- transforming as a and e, respectively. In the C_3 single-ion symmetry the ground state is ^4A and both octahedral $^4T_2$ and $^4T_1$ states split into ^4E and ^4A components. The transitions $^4A \rightarrow {}^4E$ and $^4A \rightarrow {}^4A$ are electric-dipole-allowed in σ and π polarization, respectively. Figures 1 and 2 show that the maxima of both the $^4T_2$ and $^4T_{1a}$ bands are not at exactly the same energy in π and σ polarization, the σ maximum lying lower by 230 cm^{-1} in the $^4T_2$ band and 300 cm^{-1} higher in energy in the $^4T_{1a}$ band (see also Table 2). Even if the true splittings may be slightly larger because of the presence of vibronic intensity, these values give us an estimate of the trigonal field splittings of the $^4T_2$ and $^4T_{1a}$ states in $(Et_4N)_3Cr_2F_9$, respectively. With ^4E below ^4A for $^4T_2$ and vice versa for $^4T_{1a}$, the t_0 orbital must be stabilized with respect to t_+, t_-. The splittings are small and at first sight contrast with the severe geometrical distortions of the dimer molecule from octahedral symmetry. To study the effect of the various geometrical distortions on the trigonal splittings of the quartet bands, we performed a crystal-field analysis within the framework of the angular overlap model (AOM) using the computer program Ligfield.[25] First, we restrict ourselves to the CrF_6 monomeric half of the dimer, denoting the terminal and

(25) Bendix, J. *Ligfield*, version 0.92; Department of Chemistry, University of Copenhagen: Copenhagen, Denmark.

Table 2. Comparison of Observed and Calculated Energies of Selected Absorption Bands As Indicated[a]

band	calcd, cm^{-1}		exptl, cm^{-1}
	$e_\sigma^{Cr} = 0$	$e_\sigma^{Cr} = -600$	
^4E ($^4T_2$)	14 080	14 400	14 400
^4A ($^4T_2$)	14 620	14 620	14 630
^2E (^2E)	14 760	14 810	15 000
^2E ($^2T_1$)	15 370	15 400	~15 800
^2A ($^2T_1$)	15 565	15 575	~15 800
^4A ($^4T_{1a}$)	20 820	20 820	20 950
^4E ($^4T_{1a}$)	20 920	21 240	21 250
^2A ($^2T_2$)	21 540	21 580	~21 600
^2E ($^2T_2$)	21 990	21 970	~21 600
^2A ($^2A_1$)	26 800	27 025	~26 700

[a] The values obtained from a trigonal ligand field calculation are shown in the middle, the experimental ones on the right. Bands are denoted in C_3 (O) symmetry. The following parameters were used in the calculation (see section 4.1): B, C, $e_\sigma^{F_t}$, $e_\sigma^{F_b}$, $e_\pi^{F_t}$, $e_\pi^{F_b}$, e_σ^{Cr}, θ_t, and θ_b

bridging ligands as F_t and F_b, respectively. We start from a hypothetical exact octahedron with an assumed Cr−F distance of 1.933 Å, the value found in K_2NaCrF_6.[26] The Racah parameter values are $B = 700$ cm^{-1} and $C = 3250$ cm^{-1}. The initial AOM parameters $e_\sigma^{F_{oct}}$ and $e_\pi^{F_{oct}}$ for σ and π metal−ligand bonds, respectively, were chosen such that $3e_\sigma^{F_{oct}} - 4e_\pi^{F_{oct}} = 10Dq = 14480$ cm^{-1} with $e_\pi^{F_{oct}} = 0.23e_\sigma^{F_{oct}}$,[27] yielding 6960 and 1600 cm^{-1} for $e_\sigma^{F_{oct}}$ and $e_\pi^{F_{oct}}$, respectively. In the actual dimer symmetry the angle between the trigonal axis and the terminal ligands is opened from 54.74° to $\theta_t = 58.20°$ and the Cr−F_t distance is shortened from 1.933 to 1.854 Å. On the other hand, the CrF_3Cr core is elongated along the trigonal axis, resulting in $\theta_b = 46.03°$ and a Cr−F_b distance of 1.994 Å. If the ligands are treated as point charges, $10Dq$ is proportional to r^{-5}, and the AOM parameters can thus be adapted as follows:

$$e_\lambda^{F_t} = (1.933/1.854)^5 e_\lambda^{F_{oct}} = 1.232 e_\lambda^{F_{oct}}$$

$$e_\lambda^{F_b} = (1.933/1.994)^5 e_\lambda^{F_{oct}} = 0.856 e_\lambda^{F_{oct}} \quad (1)$$

with λ being either σ or π. The resulting AOM parameter values are $e_\sigma^{F_t} = 8575$ cm^{-1}, $e_\pi^{F_t} = 1970$ cm^{-1}, $e_\sigma^{F_b} = 5960$ cm^{-1}, and $e_\pi^{F_b} = 1370$ cm^{-1}. The axial field component induced by the positive charge of the second Cr^{3+} ion in the dimer was taken into account with a parameter e_σ^{Cr}, which was varied from 0 to -1000 cm^{-1}.

The results of ligand-field energy calculations for the $^4T_2$ and $^4T_{1a}$ states with the above parameter values are compared with the experimental splittings in Table 2. Independent of the parameter e_σ^{Cr}, relatively small splittings of less than 1000 cm^{-1} are calculated for both $^4T_2$ and $^4T_{1a}$, in good agreement with the small experimental values. In view of the significant trigonal distortions this is surprising at first. But the calculations show that the effect of the trigonal elongation (large reduction of θ_b, small Cr−F_b increase) of the bridging ligands is essentially compensated by the compression of the terminal ligands (small increase of θ_t, large reduction of Cr−F_t). Table 2 shows that including the electrostatic effect of the partner Cr^{3+} ion corrects the calculated splittings in the direction of the observed ones and can thus be considered significant. The best agreement with experiment is obtained with $e_\sigma^{Cr} \approx -600$ cm^{-1}.

4.2. $^4A_2 \rightarrow {}^2A_1$ Transition. The most striking features in the spectra are the very weak, nicely resolved bands between 26 180 and 27 500 cm^{-1} (see Figure 3). They are lying between the two broad $^4T_1$ bands where usually no ligand field transitions are observed in Cr^{3+} systems. This raises the question of whether they are intrinsic or due to an impurity. Their temperature dependence corresponds to the ground-state splitting derived from the magnetic susceptibility measurement. This will be analyzed in section 4.3, and we conclude that these features belong to the $[Cr_2F_9]^{3-}$ dimer. Could they be double excitations, which are often observed in exchange-coupled systems? Although the origins of the $^4T_2$ band are not resolved in the spectra of Figure 2a, the band shape indicates that they lie below 12 700 cm^{-1}. The corresponding double excitations $^4A_2\,{}^4A_2 \rightarrow {}^4T_2\,{}^4T_2$ are thus expected to lie around 25 400 cm^{-1}, which is clearly too low compared to the lowest-energy cold band observed in the spectra at 26 262.9 cm^{-1}. Double excitations to $^2E\,{}^4T_2$ and $^2T_1\,{}^4T_2$, on the other hand, are expected above 27 700 cm^{-1}, which is definitely too high. We thus conclude that the bands between 26 180 and 27 500 cm^{-1} are single excitations of the $[Cr_2F_9]^{3-}$ pair.

For a safe assignment a trigonal ligand field calculation using the parameters reported in section 4.1 was done. The energies of all the known ligand field states are reasonably reproduced, and the $^2A_1$ state is calculated to be 27 025 cm^{-1}, which is in good agreement with the experimental value (see Figure 3 and Table 2). We therefore assign the band system between 26 180 and 27 500 cm^{-1} to the $^4A_2 \rightarrow {}^2A_1$ ($t_2 \rightarrow e$) excitation. This transition is expected to be weak and broad, which makes it difficult to observe, and to our knowledge it has never been reported so far. The following three reasons make it easier to observe this $^4A_2 \rightarrow {}^2A_1$ transition in the title compound. First, the dimer character of the chromophore leads to a general intensity enhancement of transitions that are spin-forbidden in a single ion. Second, the ligand field strength of a fluoride environment combined with the high energy of the lowest Cr−F ligand-to-metal charge transfer (LMCT) states leads to a good separation of charge transfer and ligand field states in fluorides. Figure 1 shows that in $(Et_4N)_3Cr_2F_9$ the lowest LMCT band appears at ~45 000 cm^{-1}. In the most intensively studied oxide lattices, on the other hand, $10Dq$ is larger, thus shifting $^2A_1$ to higher energy, and the lowest LMCT states are decreased to ~31000−35000 cm^{-1}. The higher-lying ligand field states are thus often swamped by the intense LMCT bands. The same happens in chloride and bromide systems, where the LMCT energies drop dramatically compared to fluorides. A third reason for the observation of $^2A_1$ in the title compound lies in the fact that it happens to fall exactly in the window between the two strong $^4T_1$ absorption bands as shown in Figure 1.

The 11 K π spectrum of $^4A_2 \rightarrow {}^2A_1$ in Figure 3 shows a detailed sideband structure built on the intense electronic origin at 26 262.9 cm^{-1}. A comparison with the 25 K spectrum indicates that the prominent sideband lines are vibrational. Additional, weaker electronic origins may be hidden in the complex vibrational sideband spectrum and therefore cannot be identified. Three fundamental molecular modes with frequencies of 313, 415, and 541 cm^{-1} are recognized, denoted as υ_1, υ_2, and υ_3 in Figure 3, respectively. Combinations of these three modes are recognized at higher energies, indicating their totally symmetric character and identifying the sideband pattern as a Franck-Condon progression with Huang−Rhys parameters S varying from 0.25 to 0.5. Since an additional unresolved sideband intensity may be hidden in the background at higher energies, these values give a lower limit for S. They are larger than for intraconfigurational transitions but unusually low for a $t_2 \rightarrow e$ one-electron excitation. For the spin-allowed $^4A_2 \rightarrow$

(26) Knox, K.; Mitchell, D. W. *J. Inorg. Nucl. Chem.* **1961**, *21*, 253.
(27) Glerup, J.; Mønsted, O.; Schäffer, C. E. *Inorg. Chem.* **1976**, *15*, 1399.

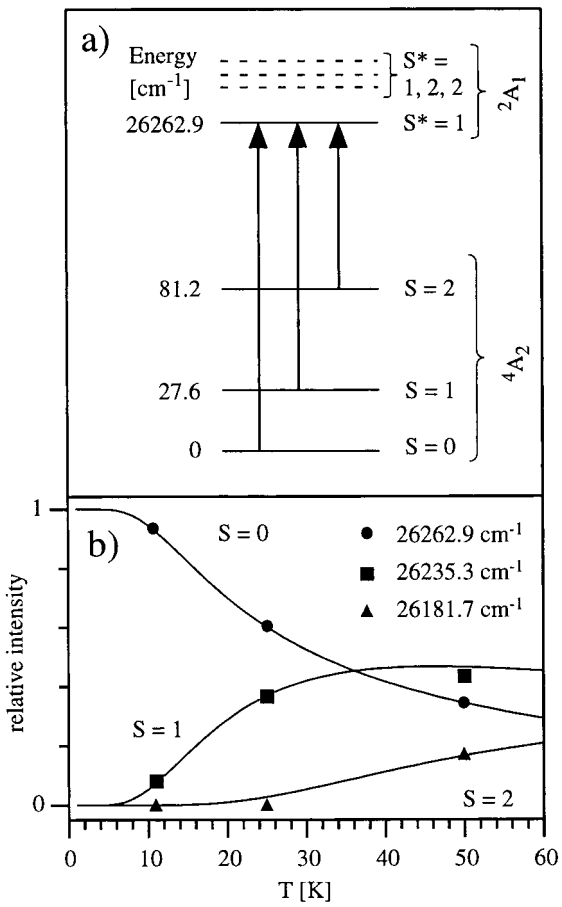

Figure 5. (a) Energy level diagram of the ground and $^2A_1$ dimer states including the observed electronic transitions from the ground-state levels. The broken lines indicate energy levels not observed at unknown energies. (b) Temperature dependence of the intensity of the π-polarized electronic $^4A_2 \rightarrow {}^2A_1$ absorption origins denoted $S = 0$, 1, and 2 at energies 26 262.9, 26 235.3, and 26181.7 cm^{-1}, respectively, compared to the Boltzmann factors (solid lines) calculated from the energy pattern in Figure 5a. The intensities are scaled to 1.

$^4T_2$ and $^4A_2 \rightarrow {}^4T_{1a}$ transitions, which are also derived from $t_2 \rightarrow e$ excitations, the unresolved band shapes indicate Huang−Rhys parameters of $S \approx 3$. The $^4A_2 \rightarrow {}^2A_1$ bands in Figure 3 exhibit a strong temperature dependence in the origin region of Figure 3, which will be analyzed in detail in section 4.3.

4.3. Optically and Magnetically Determined Dimer Splittings. Exchange interactions between the ions A and B in the $^4A_2$ ground state of a Cr^{3+} dimer can be described by the isotropic Hamiltonian

$$H = J(\mathbf{S_A}\cdot\mathbf{S_B}) - j(\mathbf{S_A}\cdot\mathbf{S_B})^2 \qquad (2)$$

where a positive value for J corresponds to an antiferromagnetic splitting. The biquadratic term leads to deviations from the regular Landé pattern expected from a Heisenberg operator. Figure 5a shows the energy splitting of these dimer levels for an antiferromagnetic interaction.

In the excited $^2A_1$ state exchange interactions lead to four dimer levels, two each with $S = 1$ and $S = 2$. Their energy splitting cannot be expressed in terms of a simple Hamiltonian as in the ground state. And since only one of these four levels could be determined experimentally, we will not go into the theory of this splitting here.

Because of the high resolution of our crystal absorption spectra, we resolve the three $^4A_2 \rightarrow {}^2A_1$ origin lines at 26 262.9, 26 235.3, and 26 181.7 cm^{-1} labeled $S = 0$, 1, and 2 in Figure 3, respectively. They have distinctly different temperature dependences as shown in Figure 5b, and we can immediately deduce the energy splitting pattern in Figure 5a. The three lines correspond to transitions from the $S = 0$, 1, and 2 dimer levels of the ground state to the same excited dimer level. This is confirmed as follows: (i) The observed temperature dependence of the absorption intensities is in excellent agreement with the Boltzmann factors calculated from this ground-state splitting (see Figure 5b). (ii) The magnetic susceptibility calculated on the basis of this energy splitting perfectly fits the experimental curve (see Figure 4). We thus have a very accurate determination of the ground-state exchange splitting, and by use of eq 2, we determine the parameter values

$$J = 25.9\ cm^{-1} \qquad j = 0.27\ cm^{-1} \qquad (3)$$

below 50 K. We note from eq 3 that the biquadratic exchange parameter j is 1.0% of J. There are various possible physical origins for j, i.e., a deviation from the simple Landé energy pattern. Reliable j values have only been determined in a few cases, and the j/J ratio is typically on the order of $^1/_{100}$ as found here.

There are two well-established intensity mechanisms for dimer transitions that are spin-forbidden in the single ion: (i) an electric-dipole single-ion mechanism that is due to the combined action of the odd-parity ligand field at the single-ion site and spin-orbit coupling, where the dimer spin selection rules for this mechanism are $\Delta S = 0, \pm 1$; (ii) an electric-dipole exchange mechanism first proposed by Tanabe and co-workers.[28] For a general pair transition involving orbital changes A ($i \rightarrow k$) and B ($j \rightarrow l$) in a dimer the interaction of the electric vector $\vec{E}$ of the incident light with the electric-dipole transition moment can be expressed as

$$H = \sum_{i,j,k,l} (\vec{\Pi}_{A_{i,k}B_{j,l}}\cdot\vec{E})(\vec{s}_{A_{i,k}}\cdot\vec{s}_{B_{j,l}}) \qquad (4)$$

where $A_{i,k}$ and $B_{j,l}$ represent the orbitals on the two metal centers and where $\vec{\Pi}_{A_{i,k}B_{j,l}}$ represents vectorial coupling coefficients related to orbital exchange parameters.[28] The dimer spin quantum number S must be conserved in this mechanism, i.e., only $\Delta S = 0$ transitions are allowed.

In our absorption spectrum we observe three lines from the $S = 0$, 1, and 2 levels of the exchange split ground state to the same dimer level of the $^2A_1$ excited state (see Figures 3 and 5). The three lines are of comparable intensity, and we conclude that the excited level has $S = 1$. We thus have two $\Delta S = \pm 1$ dimer transitions, which necessarily arise by a single-ion mechanism, and a $\Delta S = 0$ transition, which can be induced by both mechanisms. The fact that the $\Delta S = 0$ transition does not dominate shows that the Tanabe mechanism is not dominant here, in contrast to the $^4A_2 \rightarrow {}^2E$, $^2T_1$ transitions in many Cr^{3+} dimers, where $\Delta S = 0$ pair transitions are often one to 2 orders of magnitude more intense than the $\Delta S = \pm 1$ transitions. This is in good accord with the theoretical prediction that in a Cr^{3+} dimer the Tanabe mechanism is most efficient for transitions within the $(t_2)^3$ electron configuration such as $^4A_2 \rightarrow {}^2E$, $^2T_1$, whereas the $^2A_1$ excitation studied for the first time here involves a $t_2 \rightarrow e$ orbital excitation.

The $^2A_1$ excited state is split into two $S = 1$ and two $S = 2$ dimer levels by the exchange interactions. Since only transitions

(28) Ferguson, J.; Guggenheim, H. J.; Tanabe, Y. *J. Phys. Soc. Jpn* **1966**, *21*, 692.

to one of the $S = 1$ levels are identified in the absorption spectrum, we learn nothing about this excited-state exchange splitting. This is in contrast to the numerous optical studies of ^2E, $^2T_1$ excited states in Cr^{3+}, which have revealed both the ground- and excited-state splittings. The likely reason for this difference is an orbital one and lies in the $t_2 \rightarrow e$ character of the $^2A_1$ excitation. This leads to the well-developed vibrational sideband structure in Figure 3, in which some weaker origins get lost, particularly at higher temperatures. It appears that we are observing transitions to the lowest of the four exchange split levels of the $^2A_1$ state.

Interestingly, the overall dominance of π intensity in the $^2A_1$ absorption spectrum (see Figure 3) is indirectly related to the dimeric nature of the chromophore. As seen in Figure 1, the same dominance in π polarization is also observed in the two $^4T_1$ absorption bands just below and above the $^2A_1$ absorption. These $^4T_1$ excitations are the main source of intensity for the $^2A_1$ band in the single-ion mechanism, thus explaining its π dominance. The $^4T_1$ bands themselves gain their intensity by configurational mixing with ligand-to-metal and metal-to-metal ($Cr^{2+}-Cr^{4+}$) electron configurations. Transitions to the latter are an exclusive dimer property and necessarily purely π-polarized, inducing a dominance of π intensity in the $^4T_1$ bands. Similar observations were made in tri-μ-hydroxo-bridged Cr^{3+} dimers.[14]

We finally correlate the exchange splitting determined spectroscopically with the magnetic properties of the title compound. From the energy pattern in Figure 5a the temperature dependence of the magnetic susceptibility per mole of dimers is calculated as follows:[29]

$$\chi = \frac{2Ng^2\mu_B{}^2}{kT}\,\frac{e^{-E_1/kT} + 5e^{-E_2/kT} + 14e^{-E_3/kT}}{1 + 3e^{-E_1/(kT)} + 5e^{-E_2/(kT)} + 7e^{-E_3/(kT)}} + C/T \qquad (5)$$

where $E_1 = 27.6$ cm^{-1} and $E_2 = 81.2$ cm^{-1} are the experimentally determined energies of the $S = 1$ and $S = 2$ levels, respectively. $E_3 = 157.8$ cm^{-1} was calculated using $E_3 = 6J + 9j$ from eq 2 and the parameter values from eq 3. The term C/T had to be added to take account of a small paramagnetic impurity. With $g = 2.00$ and $C = 0.0337$ cm^3 K mol^{-1} the experimentally determined temperature dependence of the magnetic susceptibility is excellently reproduced. This is shown in Figure 4, where the impurity contribution is indicated as a dotted line and amounts to 0.9% of a Cr^{3+} monomeric species. The spectroscopically determined exchange splitting in Figure 5a with the parameter values in eq 3 is valid below 50 K. It is likely to decrease by a few percent upon warming to room temperature because of a slight increase of interatomic distances.[30] In the above susceptibility calculation this is taken up by the parameters g and C. The power of optical spectroscopy thus lies in the fact that it allows an accurate and direct determination of both exchange parameters J and j without having to fit a model to some bulk data.

4.4. Trends along the Series $[Cr_2X_9]^{3-}$ (X = F, Cl, Br). 4.4.1. Ground-State Exchange Parameters. In $[Cr_2X_9]^{3-}$ dimers with trigonal symmetry and neglecting biquadratic exchange the ground-state exchange parameter J is given by

$$J = \frac{1}{9}(J_a + 2J_e) \qquad (6)$$

Table 3. Comparison of J Values and Cr−Cr Distances in $(Et_4N)_3Cr_2F_9$, $Cs_3Cr_2Cl_9$ and $Cs_3Cr_2Br_9$

	$(Et_4N)_3Cr_2F_9$	$Cs_3Cr_2Cl_9$	$Cs_3Cr_2Br_9$
J, cm^{-1}	27.6	13	6.3
Cr−Cr, Å	2.769	3.12	3.316

where J_a and J_e are orbital parameters involving the t_0 and t_+, t_- orbitals transforming as a and e in C_3, respectively. They can be calculated by molecular orbital formalisms, and a ratio $J_a/J_e = 12$ was found for $Cs_3Cr_2Cl_9$.[32] We can expect this dominance of J_a to be valid for the whole series. This is nicely confirmed by the magneto-structural correlation in Table 3, where the J values for $(Et_4N)_3Cr_2F_9$, $Cs_3Cr_2Cl_9$, and $Cs_3Cr_2Br_9$ are listed together with the Cr−Cr distances. J decreases from 27.6 to 6.3 cm^{-1}, while the Cr−Cr distance increases from 2.769 to 3.312 Å. The J_a parameter mainly corresponds to the direct σ overlap of the t_0 orbitals along the Cr−Cr axis and is exponentially dependent on the Cr−Cr separation. If J_a dominates J_e, an exponential dependence of J on the Cr−Cr distance R is thus expected:[33,34]

$$J = \alpha e^{-\beta R} \qquad (7)$$

This equation provides a good reproduction of the experimental data in Table 3 with $\alpha = 2.2 \times 10^4$ cm^{-1} and $\beta = 2.4$ Å^{-1}, and we conclude that J_a is roughly an order of magnitude larger than J_e throughout the $[Cr_2X_9]^{3-}$ series.

4.4.2. ^2E and $^2T_1$ Excitations. Figure 2 compares the polarized 10 K spectra of $(Et_4N)_3Cr_2F_9$ in the region of the $^4A_2 \rightarrow {}^2E$, $^2T_1$ transitions with the corresponding 5 K spectra of $Cs_3Cr_2Cl_9$ adapted from refs 16 (high-resolution spectra) and 17. Because of the larger exchange splittings in $(Et_4N)_3Cr_2F_9$, the relative population of the ground-state levels at the indicated temperatures is approximately the same in both compounds. The intensity scale of the $Cs_3Cr_2Cl_9$ spectrum is arbitrary.

The blue shift of about 1400 cm^{-1} of the broad $^4T_2$ band is due to the stronger ligand field in $(Et_4N)_3Cr_2F_9$. The sharper features on the high-energy slope of the $^4T_2$ band are due to ^2E and $^2T_1$ excitations. As a result of larger Racah parameters B and C, they are blue-shifted by about 1000−1200 cm^{-1} in the fluoride. The general appearance of the absorption spectra in Figure 2 is similar. The overall energy range of the $^2E/^2T_1$ absorptions is about 1000 and 1500 cm^{-1} in $Cs_3Cr_2Cl_9$ and $(Et_4N)_3Cr_2F_9$, respectively. We take this as a reflection of larger exchange splittings in these excited states in the fluoride. The ^2E absorptions are broadened in both compounds. In $(Et_4N)_3Cr_2F_9$ they appear as typical antiresonance features, as observed in other Cr^{3+} systems.[35,36] They result from an interaction of the sharp $^4A_2 \rightarrow {}^2E$ transitions with the underlying broad $^4A_2 \rightarrow {}^4T_2$ absorption by spin−orbit coupling. The antiresonance character is more pronounced in the fluoride because the ^2E state lies closer to the $^4T_2$ absorption maximum, leading to stronger mixing of the $^4T_2$ and ^2E states by spin−orbit coupling.

In the region of the $^4A_2 \rightarrow {}^2T_1$ transitions the $(Et_4N)_3Cr_2F_9$ spectra show some prominent absorption lines between 15 800 and 16 000 cm^{-1} in both polarizations (see Figure 2a). They are, however, about 10 times as broad as the $^2A_1$ lines discussed

(29) Kahn, O. *Molecular Magnetism*; VCH Publishers: New York, 1993.
(30) Güdel, H. U.; Furrer, A. *Mol. Phys.* **1977**, *33*, 1335.
(31) Weihe, H.; Güdel, H. U.; Toftlund, H. *Inorg. Chem.* **2000**, *39*, 1351.
(32) Leuenberger, B.; Güdel, H. U. *Inorg. Chem.* **1986**, *25*, 181.
(33) Grey, I. E.; Smith, P. W. *Aust. J. Chem.* **1971**, *24*, 73.
(34) Niemann, A.; Bossek, U.; Wieghardt, K.; Butzlaff, C.; Trautwein, A. X.; Nuber, B. *Angew. Chem., Int. Ed. Engl.* **1992**, *31*, 311.
(35) Lempicki, A.; Andrews, L.; Nettel, S. J.; McCollum, B. C.; Solomon, E. I. *Phys. Rev. Lett.* **1980**, *44*, 1234.
(36) Bermudez, V. M.; McClure, D. S. *J. Phys. Chem. Solids* **1979**, *40*, 129.

in section 4.3 and thus do not allow as detailed an analysis. There is considerable overlap of cold and hot bands, and in contrast to $Cs_3Cr_2Cl_9$, the ground-state exchange splitting cannot be determined. However, knowledge from the analysis of the $^2A_1$ spectra allows an analysis of the complicated temperature dependence. Three π- and three σ-polarized transitions from the $S = 0$, 1, and 2 ground-state levels to different excited-state levels are derived. The results of this analysis are given in Table 1.

In conclusion, for the first time the $^4A_2 \rightarrow {}^2A_1$ excitation was resolved for any Cr^{3+} compound from the high-resolution crystal absorption spectrum of $(Et_4N)_3Cr_2F_9$ at cryogenic temperatures. This allowed a precise determination of the ground-state exchange parameters, which in turn nicely reproduce the measured temperature dependence of the magnetic susceptibility. On the other hand, only limited information could be obtained from the $^4A_2 \rightarrow {}^2E$, $^2T_1$ transitions. This is in contrast to all previous studies of the optical spectroscopic properties of Cr^{3+} dimers in which the exchange splittings were exclusively derived from the analysis of the $^4A_2 \rightarrow {}^2E$, $^2T_1$ transitions.

Acknowledgment. We thank Christian Reber (University of Montreal) for valuable discussions. Financial support from the Swiss National Science Foundation is gratefully acknowledged.

IC000759B